3-D Transonic Flow in a Compressor Cascade With Shock-Induced Corner Stall

Anton Weber
e-mail: anton.weber@dlr.de

Heinz-Adolf Schreiber
e-mail: heinz-a.schreiber@dlr.de

Reinhold Fuchs

Wolfgang Steinert

German Aerospace Center (DLR),
Institute of Propulsion Technology,
51170 Köln, Germany

An experimental and numerical study of the transonic flow through a linear compressor cascade with endwalls was conducted. The cascade with a low aspect ratio of 1.34 was tested at an inlet Mach number of 1.09 and a Reynolds number of 1.9×10^6. Detailed flow visualizations on the surfaces and five-hole probe measurements inside the blading and in the wake region showed clearly a three-dimensional boundary layer separation on the blade surface and the sidewall, and a severe corner stall induced by a strong 3-D shock system at blade passage entrance. The experimental data have been used to validate and improve the 3-D Navier-Stokes code TRACE. Results showed an excellent resolution of the complex flow field. Surface pressure distributions on the entire blade surface and the endwalls, flow angle and total pressure contours within the blade passage and the wake are compared with the experimental results. An analysis of the secondary flow of this highly staggered cascade did not show the classical corner vortex. Instead, a severe flow deviation and partly reverse flow near the walls is seen. The flow solver helped to identify a weak ring vortex that originates from the passage sidewall. Surface oil flow pictures on the blade contour and the sidewall are in qualitatively good agreement to numerical surface streaklines. A considerable improvement of the numerical results could be achieved by a gradual grid refinement, especially in the corner region and by successive code development. [DOI: 10.1115/1.1460913]

Introduction

Enormous efforts are devoted to improving the efficiency of gas turbine components. One part is to design and employ custom-tailored blade profiles with minimum losses and controlled blade boundary layers. The second and even more complex part is to minimize losses resulting from secondary flows near hub and casing. Recent three-dimensional blading design concepts, which for example apply sweep and dihedral, help to control secondary flows, to reduce or suppress corner stalls and try to avoid adverse transports of low-momentum fluids inside of the blade rows [1,2]. These complex flows can only be resolved and understood by making use of fully three-dimensional Navier-Stokes flow solvers. However, their reliability, and thus the progress of the new design approach, strongly depends on the ability to predict the flow field and the design parameters as accurately as possible, and not only to give qualitatively good results. Especially the mass flow rate, pressure rise, and efficiency strongly depend on the ability to simulate the boundary layers on blade and endwalls including 3-D separations.

Thus, there is a significant interest in thorough validations of the new Navier-Stokes solvers, especially for highly loaded flows present in compressor blade rows. Especially for transonic compressors with embedded shock waves and shock-induced separations, only a few test cases from real compressors are available, however, with limited information on viscous flow regions [3,4]. Most of the code validations have been performed with lower loaded test cases of turbine configurations with accelerated flows. Decelerated flows and separation in the corner regions are even more critical for an accurate numerical simulation.

Because of a simple geometry, steady flow, and easy experimental accessibility cascade tests allow a deep insight into the viscous flow regions and provide detailed experimental data for a thorough code validation process. Therefore, Kang and Hirsch [5], for example, analyzed a subsonic cascade with high flow turning and corner stall. They gave a detailed description of the secondary flow field and compared the results to their Navier-Stokes solutions. At very high supersonic inlet Mach numbers, Osborne et al. [6] recently provided test results of a cascade, but for compressor flows this blade had an atypical favorable pressure gradient.

The present work deals with a cascade that is typical for a transonic compressor blade section with relatively low flow turning, low supersonic inflow velocities, but a strong normal shock wave at blade passage entrance. The interaction of this shock wave with the blade boundary layer and the incoming endwall boundary layer leads to a complex flow field with shock-induced separations on the blade and the corner region.

The work presented here has two main objectives: The first objective is to analyze and understand the shock induced secondary flow from both the experiment and the numerical simulation. The second, but main, objective is to use the detailed experimental data to validate and improve the numerical algorithm, the type and density of the computational mesh, and to select suitable turbulence models of our Navier-Stokes solver. Some existing shortcomings of the simulation are discussed, although most details of the flow structure are clearly revealed.

Experimental Setup

The experiments were performed in the Transonic Cascade Tunnel of DLR Cologne. It is a closed loop, continuously running facility with an upper transonic wall and variable test section height. The air supply system enables an inlet Mach number range from 0.2 to 1.4 and a Mach number independent variation of the Reynolds number. For the present tests, in which the influence of endwall and secondary flow should be dominant, a cascade with enlarged blade chord ($c=125$ mm, $s/c=0.70$) and a relatively low aspect ratio of 1.34 was installed. Figure 1 shows the test section with four compressor blades fixed between perspex endwalls. To control inlet and exit flow of the cascade, the exit flow is guided by two tailboards combined with throttles which are hinged to the outermost blades. Although there are only four

Contributed by the International Gas Turbine Institute and presented at the International Gas Turbine and Aeroengine Congress and Exhibition, New Orleans, Louisiana, June 4–7, 2001. Manuscript received by the IGTI, October 2, 2000. Paper No. 2001-GT-345. Review Chair: R. A. Natole.

 Copyright © 2002 by ASME

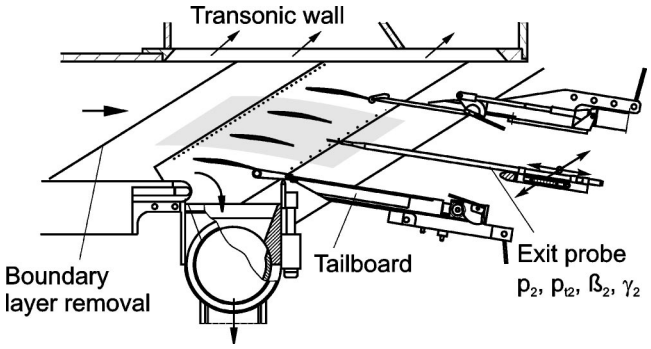

Fig. 1 Test section of DLR transonic cascade wind tunnel

blades, an acceptable periodic cascade flow could be established with suction through the outer bypass channels and a suitable throttle setting in the rear.

The blade and cascade geometry corresponds to a cascade, that has been tested extensively at DLR under 2D- and Q3D-conditions with a blade aspect ratio of 2.4 (see, for example, [7,8]) and served also as geometry in a 3-D study on blade sweep [9].

Two center blades were instrumented with static taps to measure the static pressure distribution in four spanwise sections. Furthermore, endwall static pressure distributions were recorded from 130 taps along the center blade passage (see Fig. 9). Within the blade passage and in the exit planes three and five-hole probes measured pitot- and static pressure and flow angle distributions. The 5-hole probe had a conical head with 2.6 mm in diameter. Additional laser-2-focus (L2F) readings checked inlet and exit planes and confirmed the probe results even inside of the wake regions [10].

Test Conditions. The tests were run at an inlet Mach number of 1.09, a total pressure of 1.1 bar, giving a blade chord Reynolds number of 1.9×10^6. The turbulence level of the inlet flow is approximately 0.6 percent, the thickness of the incoming sidewall boundary layer is 5 mm. Inlet flow conditions were determined from total pressure, sidewall static pressure taps and additional L2F measurements at midspan.

Description of Test Case

At a fixed inlet Mach number of 1.09 the cascade was tested at different incidence angles ranging from choked flow condition ($\beta_1=147.0$ deg) to 2.5 deg higher incidence with higher loading and stronger boundary layer separation. The test point presented here was operated with an experimental pressure ratio of 1.45, a condition at which the cascade just choked at an inlet flow angle of 147.1 deg (see Fig. 6).

Flow Structure. With the corresponding back-pressure a nearly normal shock wave establishes in front of the blade passage, but the back-pressure is high enough to avoid local reaccelerations to supersonic flows and a second normal shock. Figure 2 shows a Schlieren picture of the test section. The blade surface Mach number distributions together with the integrated midspan flow parameters are provided in Fig. 8. The Schlieren picture in reality shows integral values of the density gradients along the blade span. Dominant in this picture is the midspan location of the quasi normal shock wave ahead of the blade passage, although the shock surface near the windtunnel sidewall boundary layer is slightly bent upstream. The real three-dimensionality of the shock surface can be estimated from the simulated footprint of this shock wave which is plotted in the lower part of Fig. 3. This figure also shows the Mach contours on the sidewall and the blade suction surface.

Due to the high preshock Mach number of 1.4 near the blade surface, the shock is strong enough to induce separations. In the

Fig. 2 Schlieren photo at $M_1=1.09$, $\beta_1=147.1$ deg

blade center region a shock-induced laminar separation bubble is observed between 49 and 69 percent of chord and in the wall region a severe corner stall can be seen.

Oil flow pictures from both, the suction surface and the wall provided in Fig. 4, clearly show the region of separation, the reattachment line ($x/c=0.7$) in the center part of the blade, and the area of reverse corner flow close to the sidewalls. A sketch of the cascade and an interpretation of these surface streak lines is given in Fig. 5.

The sidewalls do not show the classical crossflow from pressure to suction side with nearwall overturning, but clearly visualize a tremendous deviation around the trailing edge and a separation line together with a focus on the rear part of the endwall. This strong deviation near the endwall in combination with a wall stall seems to be typical for cascades with high stagger angles as it was already shown in a similar, but subsonic test of Stark and Bross [11].

Simulated suction surface streak lines are plotted in the right-hand side of Fig. 4 in comparison to the experimental oil streak lines. This first comparison reveals, that the corner stall in the simulation is more extended and the footprint of the shock wave is more bowed in spanwise direction than in the experiment. Further explanations and other details in relation to the numerical result will be discussed in the forthcoming.

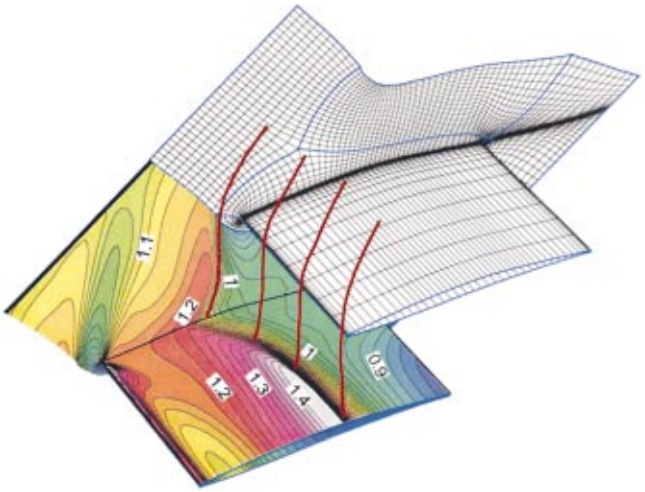

Fig. 3 Computational grid (50 percent blade span, skip=2), inlet plane: $x/c_{ax}=-0.81$, outlet plane: $x/c_{ax}=1.59$, and simulated surface iso-Mach contours at test conditions

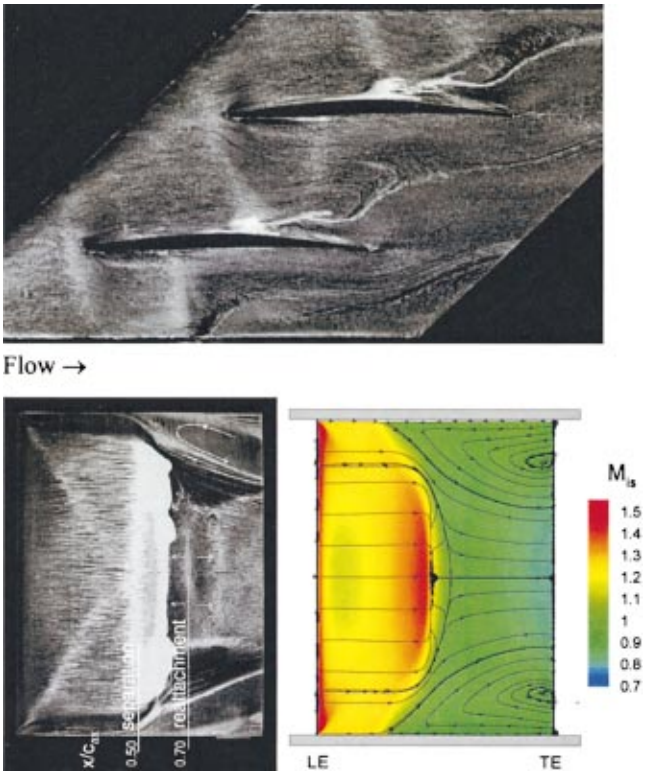

Fig. 4 Oil streak lines on sidewall (top) and suction surface (bottom, left) and TRACE simulation, $M_1=1.09$, $\beta_1=147.1$ deg

An interesting flow feature in the entrance region of this transonic flow case can be observed in the leading edge endwall corner region. The detached bow shock ahead of the leading edge interacts with the endwall boundary layer and initiates a 3-D disturbance with a slight over-expansion at the endwall leading edge corner and a weak oblique shock which both travel under about 60–65 deg toward the cascade center. The suction surface Mach number contours of the NS simulation in Fig. 4, bottom right, slightly indicate this overexpansion with peak Mach numbers in the leading edge corner region.

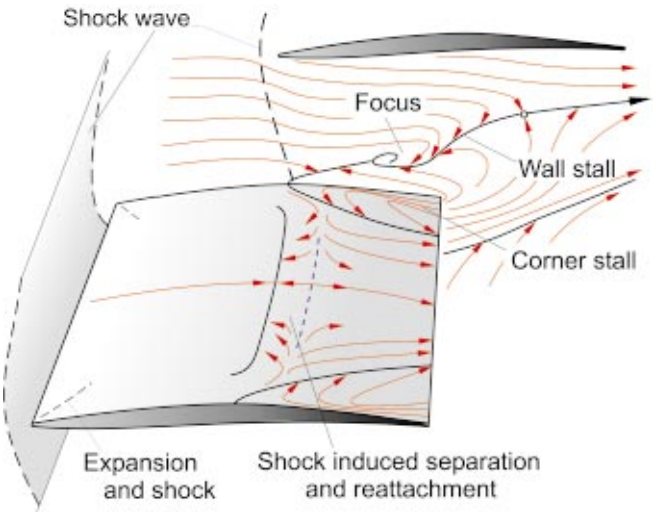

Fig. 5 Interpretation of oil streak lines

Flow Solver

The flow solver used in the numerical analysis is the 3-D Navier-Stokes code TRACE developed since 1991 at DLR Cologne for steady and unsteady turbomachinery flow simulation [12–16]. The main topics of TRACE are:

- Multi-block solver on general structured grids
- Time integration: Explicit or implicit scheme (using ILU decomposition)
- Spatial discretization: Jameson-type central differences with eigenvalue damping or Roe-upwind TVD
- Full multigrid method (FMG)—not used here.
- Steady and unsteady multistage capability using either mixing plane approach (Giles) or sheared cell technology
- Turbulence models: Baldwin & Lomax, Spalart & Allmaras, standard and low-Reynolds k-ε (Kato & Launder extension), high and low-Reynolds k-ω (extension for compressible flows, Suga, Craft & Launder approach)
- Transition modeling: Abu-Ghannam/Shaw criterion as an additional correlation—not used here.

Computational Approach

In the context of this paper the ability of the code to determine transition was not applied. All calculations were run by assuming a fully turbulent steady flow throughout the blade passage. Before starting the numerical analysis, a high-quality five-block structured grid has been generated by Yamamoto [17] and the author. Special emphasis was placed on a high degree of overall grid orthogonality and to get an ideal wake resolution, shown in Fig. 3. In order to achieve the desired inlet flow conditions M_1 and β_1 at the inlet reference plane ($x/c_{ax}=-0.25$), a constant backpressure was imposed at the outlet boundary of the computational domain at $x/c_{ax}=1.59$. Inlet and exit boundaries are treated by nonreflecting boundary conditions according to Giles and Saxer. To simulate the inlet turbulence level a mixing length of 1 percent of blade chord was imposed at the inlet plane.

The first series of calculations were performed on a relatively coarse grid having 383.823 nodal points overall, using an explicit Jameson cell-centered scheme for time integration and the standard k-ε turbulence model with wall functions. For all calculations in this mode only the relatively low loaded choked flow conditions allowed a stable and converged 3-D solution. In general, the calculated losses dominated by the strong corner stall were too high in comparison to the experiments. Therefore, the overall exit pressure level decreased by more than 5 percent—compared to the experiment—in terms of the static pressure ratio p_2/p_1. In subsequent attempts finer grids, different solution schemes as well as low-Reynolds turbulence models were applied. A major step regarding stability could be done by using an implicit upwind scheme on the basic grid. In the end, only a much finer grid with 707.119 nodal points overall ($y^+=1\ldots3$, 49 points for resolving half of the span) together with a low-Reynolds k-ω model and an implicit upwind scheme (TVD) yielded exit static pressure levels near experimental ones and stable as well as converged solutions over the whole working range. All operating points in this mode could be run with a CFL number of 100.

In contrast to the standard k-ε model with wall functions, the k-ω model used here has extensions to count for pressure dilatation, compressible dissipation, and effects of rotation. It was found that for highly loaded compressor flows the k-ω model, even with wall functions, has advantages over the standard k-ε model. Going from coarse to fine grids ends up with the same code stability and convergence behavior but less total pressure losses and higher pressure rise. Furthermore, it was found to be important to have the same fine near-surface grid spacing in the corner region, for both the blade and endwall surface.

In Fig. 6 top, the mean static pressure ratio p_2/p_1 for a constant inlet Mach number is shown as a function of the inlet flow angle

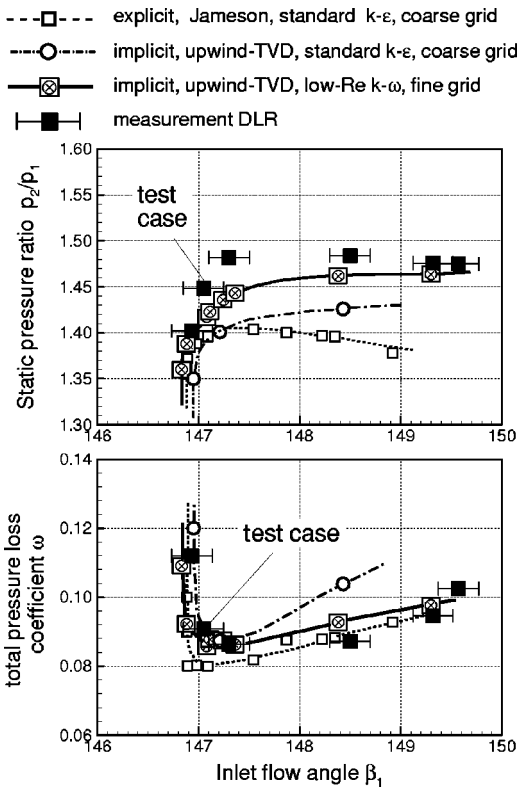

Fig. 6 Achieved overall pressure ratio and midspan total pressure losses for crucial code development steps, $M_1 \cong 1.09$.

β_1. This figure clearly illustrates the achieved static pressure ratios of the simulation for three code development steps in relation to the experimental data. The corresponding total pressure loss coefficients at blade midspan are shown in Fig. 6 bottom. In contrast to the static pressure, which is nearly constant over the whole exit plane, the total pressure varies in spanwise direction. This can be seen in Fig. 13, where for test case conditions the numerical results are compared to the experiments, one solution for a coarse grid and the other for the finest one. The largest discrepancy obviously exists in the endwall region, where the coarse grid solution (standard k-ε model, explicit scheme) shows significant higher losses. Due to higher corner losses and corresponding blockage, the coarse grid solutions provide lower overall pressure rise. It should be mentioned that the ad-hoc use of the present (up-to-date) experimental windtunnel data for code validation gave a tremendous contribution onto the code development.

Using the implicit upwind TVD scheme and the low-Reynolds k-ω turbulence model for the finest grid, the simulations for all operating points, even the near stall cases, were stable. All results presented in the forthcoming were obtained applying these latter options of the Navier-Stokes solver.

Results

For the test point, already described, with choked flow condition ($M_1 = 1.09$, $\beta_1 = 147.1$ deg) and an experimental static pressure ratio of 1.45, detailed data were collected within the blade passage and the exit plane. A second set of detailed data closer to stall exists for $\beta_1 = 148.5$ deg, but the results, which show similar agreement to the corresponding numerical simulations, are not presented here [10]. In the following sections we will concentrate on this special operating point at $\beta_1 = 147.1$ deg and compare the experimental data to the numerical analysis.

Inlet Flow. The incoming sidewall boundary layer upstream of the cascade was measured to have a thickness of 5 mm and a

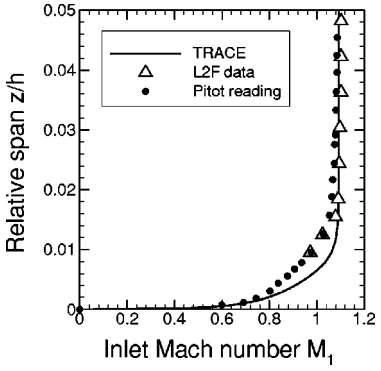

Fig. 7 Measured and simulated incoming sidewall boundary layer profiles ahead of the cascade at $x/c_{ax} = -0.25$. 3-D-NS simulation: pitchwise averaged, $M_1 = 1.09$, $\beta_1 = 147.1$ deg.

form factor of $H_{12} = 1.88$. Figure 7 shows the experimental distributions of Laser-2-Focus and pitot probe readings in comparison to the numerical simulation at a distance of 25 percent axial chord upstream of the leading edge plane. The pitchwise averaged wall boundary layer from the 3-D Navier-Stokes results shows a more ample boundary layer profile, i.e. in the simulation there is a slightly higher momentum of the incoming wall boundary layer. Nevertheless, all calculations were performed with no sidewall boundary layer imposed far upstream at the computational inlet plane ($x/c_{ax} = -0.84$), but this was done to achieve a nearly similar boundary layer thickness at the station where the wall boundary layer was measured. Imposed at the computational inlet plane were total pressure p_{t1}, total temperature T_{t1}, a constant inlet turbulent intensity of 1 percent, and the pitchwise velocity component v_1, which is known via the target values M_1 and β_1.

Mach Number Contours. In Fig. 8 calculated and measured blade surface Mach numbers are compared in 4 spanwise sections at 7.1, 16.7, 27.4, and 50 percent span from the sidewall. At the top of Fig. 8 inlet and exit mean values at midspan are listed. Here, the overall agreement is quite good. Differences occur in the static pressure ratio, where the simulation could not just reach the experimental value of $p_2/p_1 = 1.45$ and the exit flow angle β_2, where in the experiment a 0.8 deg higher flow turning is measured. In the lower part experimental (left) and simulated (right) profile Mach numbers in 4 cuts are presented. It is clearly shown that from mid-span toward the sidewall the shock front moves upstream for both, theory and experiment. The theory, however, slightly overpredicts this upstream movement of the 3-D shock surface, which can be seen in the footprints of the shock in the lower part of Fig. 4. On the pressure side there is only little variation in the isentropic Mach number distribution in spanwise direction due to a local incidence increase when approaching the wall.

In the center of Fig. 8, experimental and numerical surface Mach numbers are compared in a section near the sidewall and at midspan. In general, there is a good agreement for both cuts. Both show a higher local incidence close to the wall in relation to the midspan section and both have less pressure increase near the wall. But as the simulation achieves a lower back-pressure than the experiment, there is a slight difference between the simulated and measured isentropic Mach number levels in the rear part of the passage. At midspan, the flow acceleration on the suction side leads to a so-called preshock overshoot ($M_{max} = 1.46$), whereas in the experiment there is a flattening of the distribution caused by a laminar shock-induced separation with a maximum Mach number of only 1.34. The shock-induced (laminar) separation extends from 49–69 percent with a turbulent reattachment indicated by vertical dotted lines. In contrast to that the numerical turbulent simulation found a short turbulent separation bubble from 50–54 percent of chord. An additional experiment outside of this project,

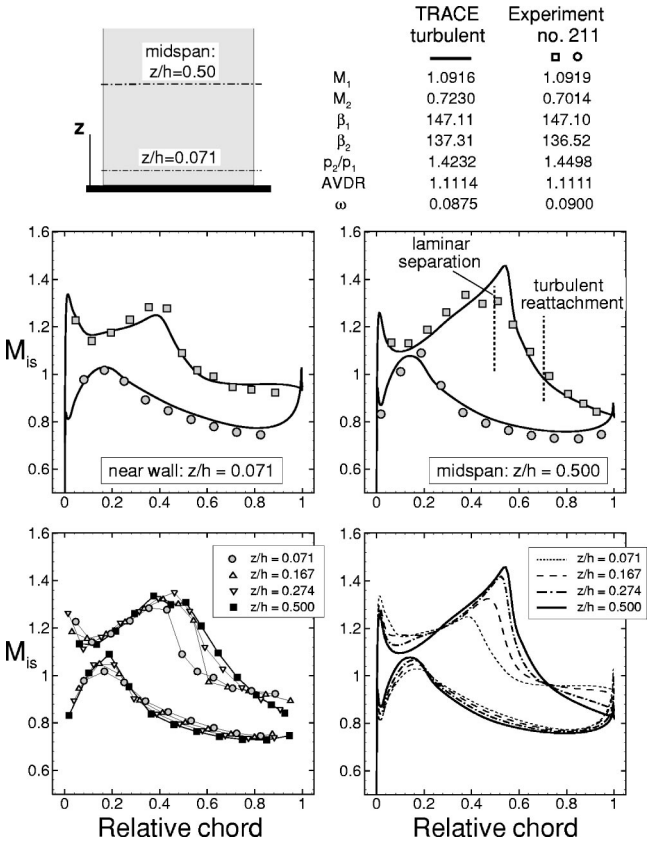

Fig. 8 Isentropic profile Mach number distribution in 4 spanwise cuts. Top: averaged data at midspan; center: near-wall and midspan distributions; bottom: spanwise development in experiment and 3-D simulation.

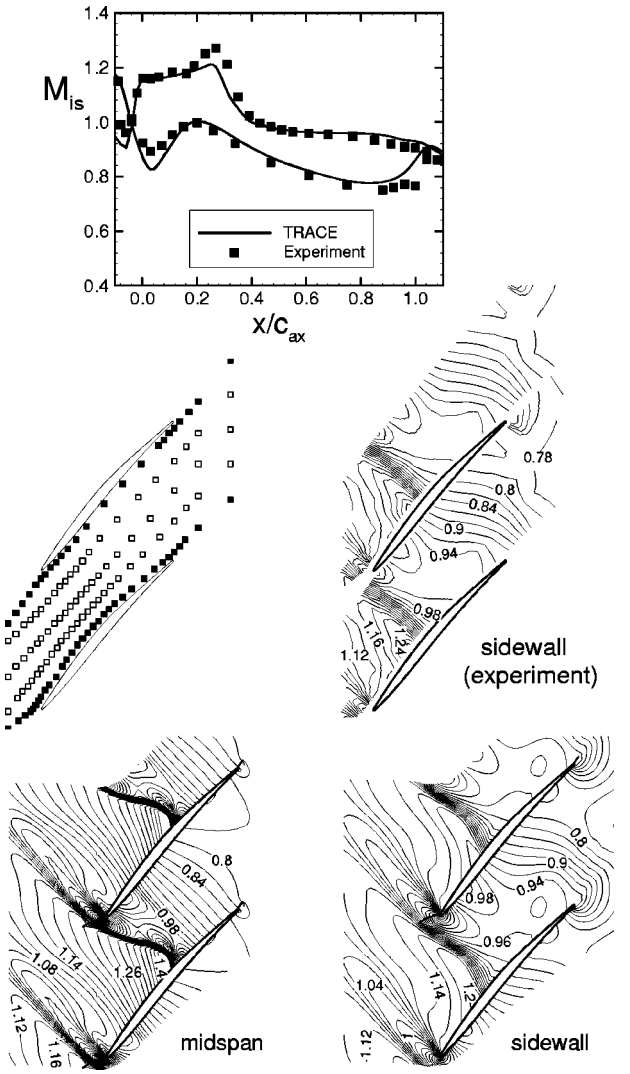

Fig. 9 Isentropic Mach number. Top: distribution near SS and PS sidewall/corner (full symbols in pressure tap locations); center right: experimental contours from sidewall pressure taps; bottom: 3-D simulation at midspan and sidewall.

in which the suction surface boundary layer was forced to become turbulent ahead of shock impingement, showed less upstream influence underneath the shock, and thus a slightly higher preshock Mach number similar to the presented numerical result. Improvements in calculating the present laminar shock induced separation are achieved by assuming a laminar profile boundary layer together with a transition model, a first result of which is presented by Kügeler et al. [15].

In the experiment the sidewall of one blade passage was equipped with 130 static pressure taps, as can be seen at the center of Fig. 9 left. At right, the measured isentropic Mach number contours are plotted. The experiment shows a nearly normal shock which meets the suction surface at 40 percent of chord. In contrast to that, the numerical analysis (bottom, right) shows a curved shock front with more upstream influence near the blade surface. In the trailing edge region again the theoretical Mach number level is slightly higher—compare, for example, $M_{is}=0.94$ at the sidewall. At midspan, the simulated iso-Mach lines can be seen at bottom, left. The shock front is shifted more downstream in comparison to the sidewall, especially near the shock impingement point at the suction surface and the shock front is strongly bowed. At the top of Fig. 9 the wall Mach number distribution along two near-blade cuts (full symbols at center, left) is shown and the corresponding numerical results are interpolated into the experimental pressure tap locations. In the simulation, again, the near-wall shock position is slightly shifted more upstream with lower preshock Mach numbers in comparison to the experiment.

S_3 Traverses. Figure 10 shows total pressure contours from two S_3 traverse planes ($x=$constant) inside of the cascade at $x/c_{ax}=0.71$ and 0.86 and one plane in the wake region at $x/c_{ax}=1.43$, which is identical to the denoted cascade exit plane 2. Inside of the cascade a large separation in the suction side corner with a symmetrical quarter-circle-like shape can be seen in the numerical analysis. Unlike in the experiment the low total pressure zone is more extended along the wall in pitchwise direction toward the pressure side and less extended in spanwise direction; i.e., there is a more triangularlike shape, measured also by Stark and Bross [11]. In both passage traverses the spatial extension of the reverse flow region is marked with a dotted line in the simulation. The thickness of the calculated suction side boundary layer decreases slightly from midspan toward the region about 20 percent from the wall. This region of minimal viscous losses is accompanied by minimal shock losses (blue areas in Fig. 10), a region in which the main shock wave is pushed forward and becomes oblique due to the interaction with the endwall boundary layer. Both effects, less shock losses and even more clearly, less viscous losses around $z/h=0.2$ are also recognized by the pitot probe measurements.

Downstream of the trailing edge plane, both theory and experiment show a similar mixing behavior of blade wake. Due to a tremendous deviation in the near-wall region, the wake center line is curved and shifted toward the pressure side. However, as the corner stall was more pronounced in the simulation, the region of low total pressure is still more concentrated in this area.

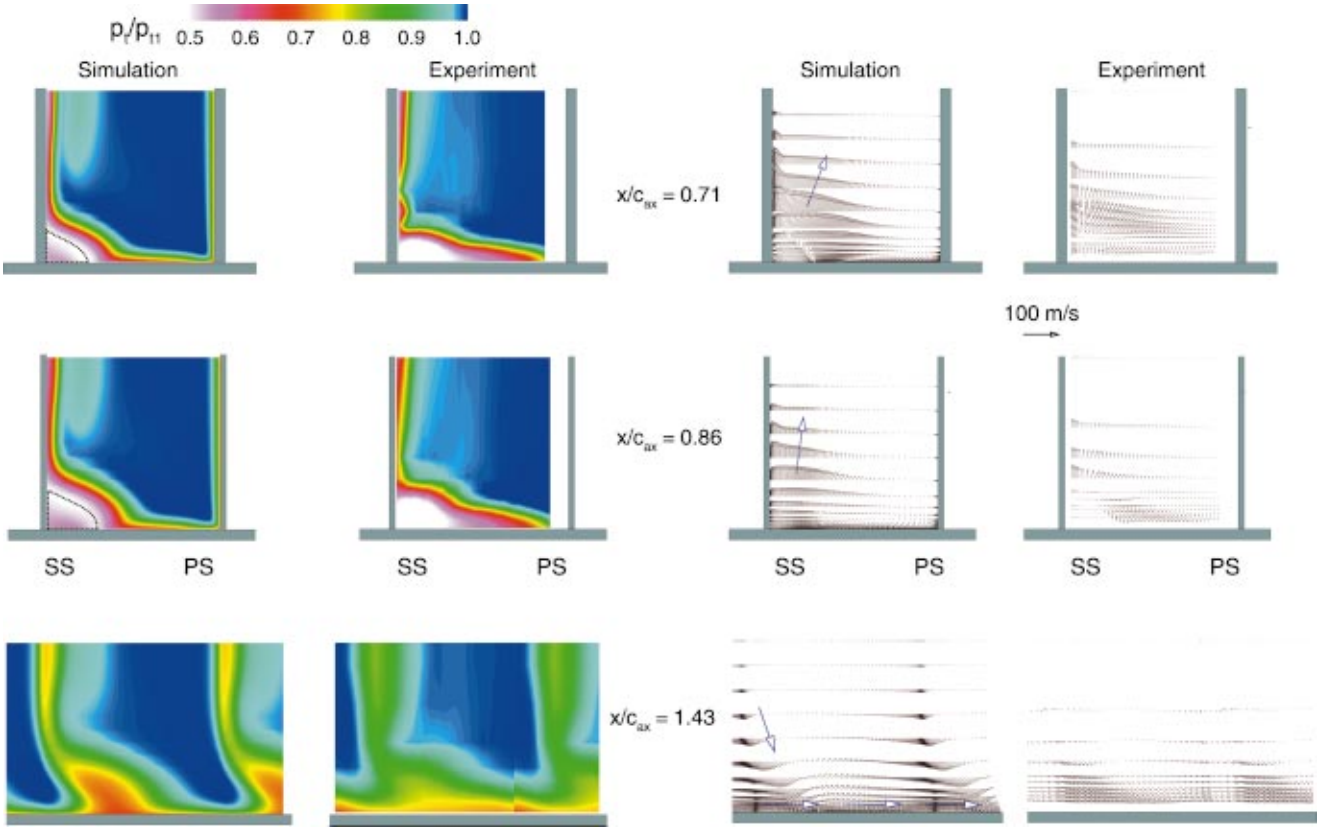

Fig. 10 Development of total pressure in streamwise direction and extension of reverse flow region (dotted line), left 3-D simulation, right experiment (Pitot probe)

Fig. 11 Development of secondary velocity in streamwise direction, right-hand side: five-hole probe experiment

In the same axial positions calculated and measured secondary flow charts are shown in Fig. 11. Neither inside of the cascade nor in the wake traverse can a classical passage vortex pattern be detected. The dominant secondary flow inside of the blading takes a direction away from the suction side corner; i.e., mass is transported mainly toward midspan. In the exit traverse plane there are two dominant secondary flow directions. Globally, the mixing of the low-momentum blade wake forces the mean flow to fill up the blade wake, and especially the former suction side corner region. Therefore, there is a mass transport toward the sidewall, but in the direct vicinity of the sidewall the secondary flow is directed in bladewise direction from suction to pressure side which is just the opposite direction of a classical passage vortex. This phenomenon was already analyzed experimentally by Stark and Bross [11] for highly staggered compressor cascades. The comparison theory versus experiment shows an overall similar flow pattern, but the magnitude of the secondary velocity vectors is at least 20 percent higher in the numerical simulation.

Intrablade Spanwise Sections. For a quantitative comparison of local experimental and simulated flow data Fig. 12 shows a series of plots with total pressure, pitchwise and spanwise flow angle distributions (β and γ) along z=constant cuts in the rear part of the blade passage ($x/c_{ax}=0.86$). For the total pressure both Pitot and five-hole probe readings are compared with the numerical analysis. At midspan position and 29.8 percent span away from the wall, the 3-D simulation and the experimental data agree quite well. Significant differences are observed at $z/h=0.149$ in the total pressure distributions and the spanwise flow angle distributions γ. This is due to the fact that in the numerical analysis this cut is placed already within the corner stall region, whereas in the experiment this cut is just aside. Because of more corner blockage in the simulation there is also more spanwise mass transport toward the blade center, indicated by higher values in the γ-distribution at $z/h=0.149$. At the wall-nearest cut at $z/h=0.071$, the flow angle determinations of the numerical simulation, both β and γ, are doubtful, because this cut is located just near the center of the corner stall and in a region of partly reverse flow, where the data analysis fails. This uncertainty is true also for the flow angle measurements within this reverse flow region. Also, the near suction surface five-hole probe measurements of the β-angle are imperfect and had to be corrected.

Spanwise Flow Quantities. Figure 13 shows spanwise distributions for conservatively averaged total pressures and flow angles β at the exit plane at $x/c_{ax}=1.43$. This was done by mixing out pitchwise variations in flow properties via solving the conservation equations for mass, momentum, and energy for both theory and experiment. The total pressure has a slight minimum around 20–25 percent of span before it increases toward the wall (see again center of Fig. 10). Approaching the sidewall, the exit flow angle shows a continuous increase of deviation up to more than 15 deg. As already mentioned before, a comparable result was obtained by Stark and Bross [11], who measured a similar flow angle distribution also behind a highly staggered compressor cascade. The classical overturning near the cascade endwalls, that normally results from crossflow emerging from pressure to suction side and the corresponding passage vortex, obviously exists only with compressor cascades of low stagger angle and higher overall flow turning, which can be seen for example in Kang and Hirsch [5]. In the present highly staggered cascade, the boundary layer separation on the sidewall effectively suppresses the cross flow and the corresponding local overturning. Both the oil flow traces on the sidewall in Fig. 4 and their interpretation in Fig. 5 show this line of wall separation diagonally in the rear part of the passage.

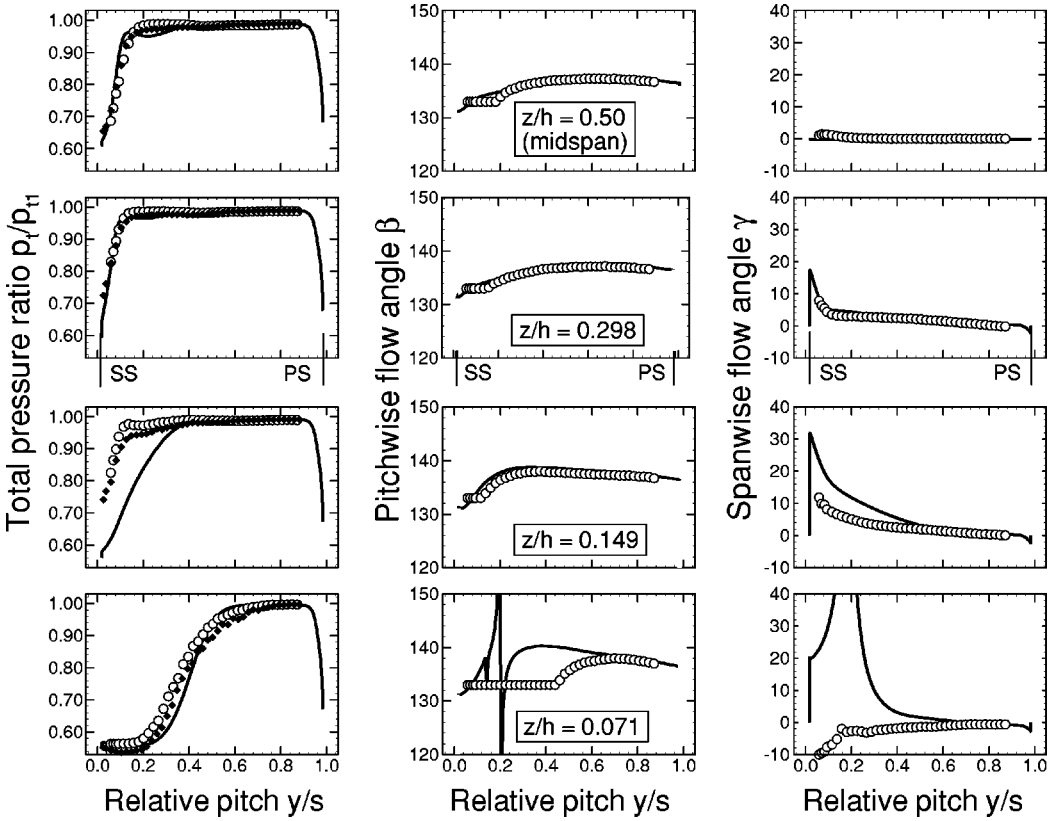

Fig. 12 Pitchwise distribution of total pressure and flow angles β and γ inside the blade passage ($x/c=0.86$) at four spanwise positions. 3-D-simulation compared to experimental data from 5 hole probe (hollow) and extra Pitot readings (solid symbols).

Structure of Corner Stall

The typical horseshoe vortex that normally forms around the blade leading edge is practically not visible and seems to have no significant influence on the endwall- and global passage flow. The flow ahead of the leading edge is just primarily influenced by the interaction of the detached bow shock with the incoming endwall

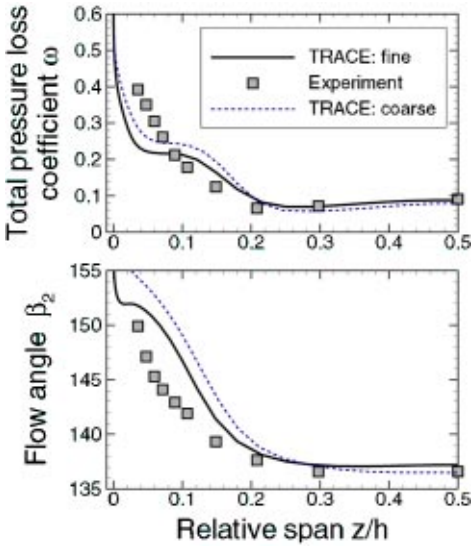

Fig. 13 Spanwise distributions in exit plane at $x/c_{ax}=1.43$, pitchwise averaged. Coarse grid: standard k-ε model with wall functions; fine grid: low Reynolds k-ω model.

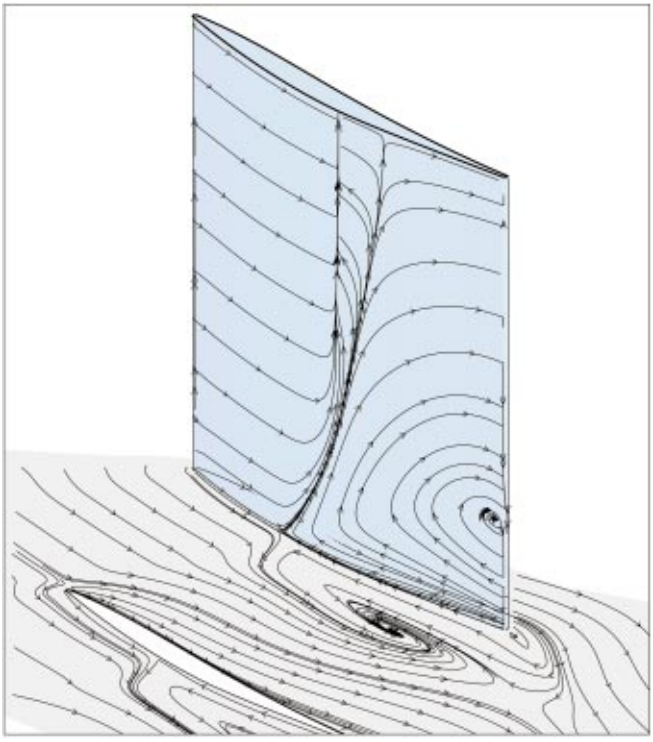

Fig. 14 Simulated surface streak lines on blade and sidewall

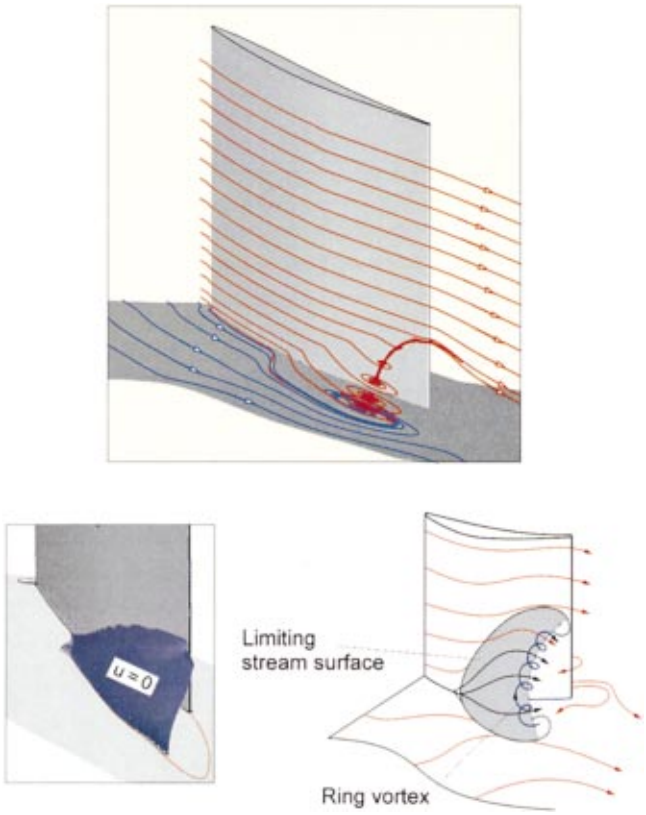

Fig. 15 Simulated near-wall streamlines on suction surface and sidewall—bottom left: calculated structure of reverse flow

boundary layer, the effect of which is hardly visible as a slight disturbance on the wall and suction surface oil traces in Fig. 4. The rear part of the blade passage, however, is dominated by the corner stall and associated wall stall. The experimental Oil streak lines on sidewall and suction surface in Fig. 4 clearly show the reverse flow regions and the stall line on the wall. The numerical Navier-Stokes simulation of surface flow traces shown in Fig. 14 provides very similar results. Experiment and simulation both visualize the endwall separation line that rolls up into a focus and the reverse flow around the trailing edge. On the suction surface, especially in the corner region, the streaklines are somewhat different. Again, the stall region in the simulation is a bit more extended and shows a small focus at the trailing edge which is not visible in the experiment (Fig. 4, bottom).

For a better and complete understanding of the complex flow pattern, especially away from the surface and inside the separation region, solely flow visualizations of the surface streak lines are not sufficient. Probes and even laser anemometers are in most cases unsuitable tools to study the complex stall regions and vortex structures. A thorough analysis of the three-dimensionally simulated flow field can fill this gap. Therefore, particle traces were generated from the numerical solutions which started at the entrance region of the cascade. For an optimal visualization of the vortex topology it was necessary to start the sidewall traces just inside the boundary layer and the blade surface traces just outside of the shear layer. Within the corner stall region the corresponding traces from both sides roll up to a vortex shown in the upper part of Fig. 15. One end of this vortex originates from the sidewall and the outer leg just hits the trailing edge. In further experiments and numerical simulations, however, we observed that the detailed structure of this vortex strongly depends on the operating condition and especially on the back pressure, as was also discussed in a similar work of Hah and Loellbach [18], who analyzed a corner stall in a compressor stator hub region and a similar corner stall in the hub region of the NASA rotor 37. In the present experiments the ring-like vortex is shifted upstream when the back-pressure is increased and with lower back pressure it seems that the outer branch of the vortex away from the wall points downstream.

In contrast to the present Navier-Stokes simulation (see Fig. 4, bottom right), in the experiment shown here the outer branch of the vortex does not meet the profile trailing edge (Fig. 4, bottom left), but probably drifts toward the wake region. Basically, however, the topology of this shock-induced corner stall is well predicted and very similar to the topology already suggested by Schulz et al. [19]. The sketch in the lower part of Fig. 15 right again illustrates the limiting stream surface above the separation zone and the ring vortex that originates from the wall. On the left-hand side of this figure, the extension of the reverse flow region of the present test case is demonstrated by the calculated stream-surface with $u=0$.

Conclusions

A detailed experimental and numerical study on shock-induced corner and wall stall in a linear compressor cascade has been presented. The Navier-Stokes simulation provided an excellent resolution of the flow field, showing up many details like surface streaklines, shock-induced separation and the vortex structure within the corner region. Simulation and experiment both showed clearly that with this highly staggered cascade there is no cross-flow on the sidewall from pressure to suction side and no corresponding overturning near the wall. Thus, no classical passage vortex exists, but instead a weak ring vortex originates from a separation region on the rear part of the sidewall.

During the code validation process, the numerical results of the Navier-Stokes solver were improved by:

- grid refinements especially in the corner regions,
- applying a low-Reynolds k-ω turbulence model,
- introducing an implicit upwind scheme (TVD)

Although the results were improved considerably, the simulation still slightly overpredicts the extension of the corner stall and the resulting blockage effect. Because of that, the simulation achieved less static pressure rise than the experiment. Further improvements are expected by considering laminar flow on the blade front and transition in the shock interaction region.

Overall, the work presented above demonstrated the fruitful interplay between computational and experimental fluid mechanics. In this context, the present Navier-Stokes solver was improved and validated especially for flows in compressors with strong decelerations and complex corner separations.

Remarks. A collection of selected data of this test case is published in a short report of Weber et al. [20] and available via Internet: http://www.dlr.de/~toni/tsg97.htm.

Acknowledgments

This work was partially supported by Arbeitsgemeinschaft Hochtemperatur-Gasturbine (AG Turbo), Bundesministerium für Wirtschaft und Technologie, BMWi, Förderkennzeichen 0327040B5.

Nomenclature

AVDR = axial velocity density ratio: AVDR$=(\rho_2 u_2)/(\rho_1 u_1)$
c = chord length
h = blade height
M = Mach no.
p = pressure
Re = Reynolds no.
s = blade spacing
u,v,w = cartesian velocity components

x,y,z = cartesian coordinates (x: axially, y: pitchwise, z: spanwise)
β = pitchwise flow angle: $\beta = \text{atan}(v/u) + 90$ deg
γ = spanwise flow angle $\gamma = \text{atan}(w/u)$
ρ = density
ω = total pressure loss coefficient: $\omega = (p_{t1} - p_t)/(p_{t1} - p_1)$

Subscripts

1 = inlet plane upstream of leading edge: $x/c_{ax} = -0.25$
2 = exit plane downstream of trailing edge: $x/c_{ax} = 1.43$
ax = axially
is = isentropic entity
LE = leading edge
t = total
TE = trailing edge

References

[1] Weingold, H. D., Neubert, R. J., Behlke, R. F., and Potter, G. E., 1997, "Bowed Stators: An Example of CFD Applied to Improve Multistage Compressor Efficiency," ASME J. Turbomach., **119**, pp. 161–168.

[2] Gümmer, V., Wenger, U., and Kau, H. P., 2001, "Using Sweep and Dihedral to Control Three-Dimensional Flow in Transonic Stators of Axial Compressors," ASME J. Turbomach., **12**, Paper No. 2000-GT-491.

[3] Fottner, L., 1990, "Test Cases for Computation of Internal Flows in Aero Engine Components," AGARD-AR-275.

[4] Dunham, J., 1998, "CFD Validation for Propulsion System Components," AGARD-AR-355.

[5] Kang, S., and Hirsch, Ch., 1991, "Three Dimensional Flow in a Linear Compressor Cascade at Design Conditions," ASME Paper No. 91-GT-114, Orlando, FL.

[6] Osborne, D. J., Ng, W. F., and Tweedt, D. L., 1998, "Studies of Secondary Flow at Endwall of a Supersonic Compressor Cascade," AIAA J., **36**, No. 2, pp. 128–133.

[7] Steinert, W., Schreiber, H. A., and Weber, A., 1996, "Experimente am transsonischen Verdichtergitter DLR-TSG-89-5 bei $M_1 = 0.90$ und $M_1 = 1.09$," DLR-IB-325-10-96, DLR Köln, Germany.

[8] Fuchs, R., Steinert, W., and Starken, H., 1993, "Transonic Compressor Rotor Cascade with Boundary-Layer Separation: Experimental and Theoretical Results," ASME Paper No. 93-GT-12-405.

[9] Weber, A., and Nicke, E., 1997, "A Study of Sweep on the Performance of a Transonic Cascade with and without Endwall Influence," Proc., 13th Int. Symp. Air Breathing Engines, ISABE, Chattanooga, TN, Vol. 2, pp. 877-888.

[10] Weber, A., Schreiber, H. A., Fuchs, R., and Steinert, W., 2000, "Räumliche Strömungen in transsonischen Verdichtergittern sehr hoher Belastung," Abschlußbericht zum HTGT-Turbotech Vorhaben 1.131 der Arbeitsgemeinschaft Hochtemperatur-Gasturbine (AG-Turbo), DLR Köln, Germany.

[11] Stark, U., and Bross, S., 1996, "Endwall Boundary Layer Separations and Loss Mechanisms in Two Compressor Cascades of Different Stagger Angle," AGARD-CP-571, Paper No. 1.

[12] Vogel, D. T., 1994, "Navier-Stokes Calculation of Turbine Flows with Film Cooling," 19th Congress of the International Council of the Aeronautical Sciences, ICAS-94-12-253.

[13] Vogel, D. T., 1999, "A Simulation Package for Turbomachinery Components," Proc. First ONERA-DLR Aerospace Symposium, Paris, France.

[14] Kügeler, E., 2000, "Numerische Untersuchung der Filmkühlung aus einer Reihe von Fan-shaped Bohrungen auf der Saugseite einer Turbinenschaufel und Vergleich mit Experimenten," DGLR Jahrestagung 2000, Leipzig, DGLR-JT2000-139, Bonn, Germany.

[15] Kügeler, E., Weber, A., and Lisiewicz, S., 2001, "Combination of a Transition Model with a Two-Equation Turbulence Model and Comparison with Experimental Results," Proc. 4th European Turbomachinery Conference, Florence, Italy, Paper No. ATI-CST-076/01.

[16] Eulitz, F., Engel, K., Nürnberger, D., Schmitt, S., and Yamamoto, K., 1998, "On Recent Advances of a Parallel Time-Accurate Navier-Stokes Solver for Unsteady Turbomachinery Flow," *Computational Fluid Dynamics '98*, Proc., 4th ECCOMAS, eds., Papailiou et al., Vol. 1, Part 1, pp. 252–258, John Wiley & Sons, New York, NY.

[17] Yamamoto, K., and Engel, K., 1997, "Multiblock Grid Generation Using an Elliptic Differential Equation," AIAA Paper No. 97-0201, 35th Aerospace Sciences Meeting & Exhibit, Reno, NV.

[18] Hah, C., and Loellbach, J., 1999, "Development of Hub Corner Stall and Its Influence on the Performance of Axial Compressor Blade Rows," ASME J. Turbomach., **121**, pp. 67–77.

[19] Schulz, H. D., Gallus, H. E., and Lakshminarayana, B., 1989, "Three-Dimensional Separated Flow Field in the Endwall Region of an Annular Compressor Cascade in the Presence of Rotor-Stator Interaction—Part I: Quasi-Steady Flow Field and Comparison with Steady-State Data," ASME Paper No. 89-GT-76.

[20] Weber, A., Steinert, W., Fuchs, R., and Schreiber, H. A., 1999, "3D Flow in a Transonic Compressor Cascade (DLR TSG-97)," DLR-IB-325-06-99.